

Quantum Well Infrared Photodetector Research and Development at Jet Propulsion Laboratory

S. D. Gunapala, S. V. Bandara, J. K. Liu, W. Hong, E. M. Luong, J. M. Mumolo,
M. J. McKelvey, D. K. Sengupta, A. Singh^a, C. A. Shott^b ~~and~~ R. Carralejo^b, *T.N.*
Krabach, J.T. Bock, M. Ressler, and M. Werner

Center for Space Microelectronics Technology, Jet Propulsion Laboratory, California Institute of
Technology, Pasadena, CA

^aAir Force Research Laboratory, Kirtland Air Force Base, NM

^bAmber, A Raytheon Company, Goleta, CA

Keywords: Quantum wells, infrared detectors, focal plane arrays, dualband detectors, broadband detectors, applications

ABSTRACT

One of the simplest device realizations of the classic particle-in-the-box problem of basic quantum mechanics is the Quantum Well Infrared Photodetector (QWIP). In this paper we discuss the optimization of the detector design, material growth and processing that has culminated in realization of 15 micron cutoff 128x128 QWIP focal plane array camera, hand-held and palmsize 256x256 long-wavelength QWIP cameras and 648x480 long-wavelength cameras, holding forth great promise for myriad applications in 6-25 micron wavelength range in science, medicine, defense and industry. In addition, we present the recent developments in broadband QWIPs, mid-wavelength/long-wavelength dualband QWIPs, long-wavelength/very long-wavelength dualband QWIPs, and high quantum efficiency QWIPs for low background applications in 4-26 μm wavelength region for NASA and DOD applications.

1. INTRODUCTION

There are many applications that require long wavelength, large, uniform, reproducible, low cost, low 1/f noise, low power dissipation, and radiation hard infrared (IR) focal plane arrays (FPAs). For example, the absorption lines of many gas molecules, such as ozone, water, carbon monoxide, carbon dioxide, and

nitrous oxide occur in the wavelength region from 3 to 18 μm . Thus, IR imaging systems that operate in the long wavelength IR (LWIR) region (8 - 18 μm) are required in many space applications such as monitoring the global atmospheric temperature profiles, relative humidity profiles, cloud characteristics, and the distribution of minor constituents in the atmosphere which are being planned for NASA's Earth Observing System ¹. In addition, 8-15 μm FPAs would be very useful in detecting cold objects such as ballistic missiles in midcourse (when hot rocket engine is not burning most of the emission peaks are in the 8-15 μm IR region) ². The GaAs based Quantum Well Infrared Photodetector (QWIP) ³ is a potential candidate for such space borne applications and it can meet all of the requirements mentioned above for this spectral region.

A quantum well designed to detect infrared (IR) light is called a quantum well infrared photodetector (QWIP). An elegant candidate for QWIP is the square quantum well of basic quantum mechanics ³. When the quantum well is sufficiently deep and narrow, its energy states are quantized (discrete). The potential depth and width of the well can be adjusted so that it holds only two energy states: a ground state near the well bottom, and a first excited state near the well top. A photon striking the well will excite an electron in the ground state to the first excited state, then an externally-applied voltage sweeps it out producing a photocurrent. Only photons having energies corresponding to the energy separation between the two states are absorbed, resulting in a detector with a sharp absorption spectrum. Designing a quantum well to detect light of a particular wavelength becomes a simple matter of tailoring the potential depth and width of the well to produce two states separated by the desired photon energy. The GaAs/Al_xGa_{1-x}As material system allows the quantum well shape to be tweaked over a range wide enough to enable light detection at wavelengths longer than $\sim 6 \mu\text{m}$. Fabricated entirely from large bandgap materials which are easy to grow and process, it is now possible to obtain large uniform FPAs of QWIPs tuned to detect light at wavelengths from 6 to 25 μm in the GaAs/Al_xGa_{1-x}As material system ³.

Improving QWIP performance depends largely on minimizing the parasitic current that plagues all light detectors, the dark current (the current that flows through a biased detector in the dark, i.e., with no

2. TEST STRUCTURE RESULTS (14-15 MICRONS)

The device structure consists of 50 periods containing 65 Å wells of GaAs (doped $n = 2 \times 10^{17} \text{ cm}^{-3}$) and 600 Å barriers of $\text{Al}_{0.15}\text{Ga}_{0.85}\text{As}$ (sandwiched between 0.5 μm GaAs top and bottom contact layers doped $n = 2 \times 10^{17} \text{ cm}^{-3}$) grown on a semi-insulating GaAs substrate by molecular beam epitaxy (MBE). Then a 1.1 μm thick GaAs cap layer on top of 300 Å $\text{Al}_{0.15}\text{Ga}_{0.85}\text{As}$ stop-etch layer was grown *in situ* on top of the device structure to fabricate the light coupling optical cavity. The MBE grown QWIP structure was processed into 200 μm diameter mesa test structures (area = $3.14 \times 10^{-4} \text{ cm}^2$) using wet chemical etching, and Au/Ge ohmic contacts were evaporated onto the top and bottom contact layers. The responsivity spectra of these detectors were measured using a 1000 K blackbody source and a grating monochromator. The absolute peak responsivities (R_p) of the detectors were measured using a calibrated blackbody source. The detector were back illuminated through a 45° polished facet³ and its responsivity spectrum is shown in Fig. 2. The responsivity of the detector peak at 14.2 μm and the peak responsivity (R_p) of the detector is 420 mA/W. The spectral width and the cutoff wavelength are $\Delta\lambda / \lambda = 13\%$ and $\lambda_c = 14.9 \text{ μm}$.

3. TEST STRUCTURE RESULTS (8-9 MICRONS)

Each period of the multi-quantum well (MQW) structure consists of a 45 Å well of GaAs (doped $n = 4 \times 10^{17} \text{ cm}^{-3}$) and a 500 Å barrier of $\text{Al}_{0.3}\text{Ga}_{0.7}\text{As}$. Stacking many identical quantum wells (typically 50) together increases photon absorption. Ground state electrons are provided in the detector by doping the GaAs well layers with Si. This photosensitive MQW structure is sandwiched between 0.5 μm GaAs top and bottom contact layers doped $n = 5 \times 10^{17} \text{ cm}^{-3}$, grown on a semi-insulating GaAs substrate by molecular beam epitaxy (MBE). Then a 0.7 μm thick GaAs cap layer on top of a 300 Å $\text{Al}_{0.3}\text{Ga}_{0.7}\text{As}$ stop-etch layer was grown *in situ* on top of the device structure to fabricate the light coupling optical cavity.

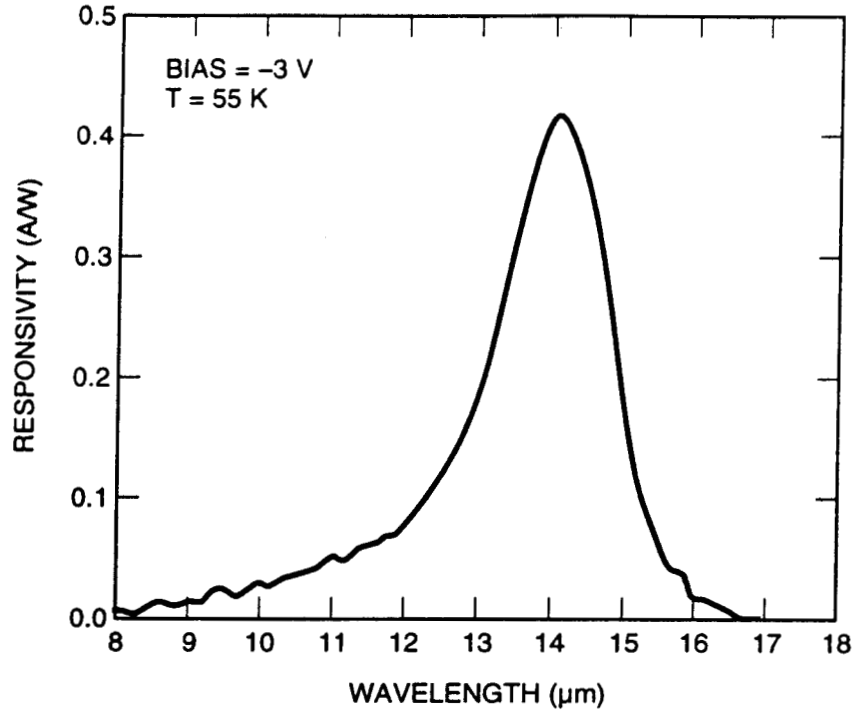


Fig. 2. Responsivity spectrum of a bound-to-quasibound VWIR QWIP test structure at temperature $T = 55$ K. The spectral response peak is at $14.2 \mu\text{m}$ and the long wavelength cutoff is at $14.9 \mu\text{m}$.

The detectors were back illuminated through a 45° polished facet as described earlier and a responsivity spectrum is shown in Fig. 3. The responsivity of the detector peaks at $8.5 \mu\text{m}$ and the peak responsivity (R_p) of the detector is 300 mA/W at bias $V_B = -3 \text{ V}$. The spectral width and the cutoff wavelength are $\Delta\lambda / \lambda = 10\%$ and $\lambda_c = 8.9 \mu\text{m}$ respectively. The measured absolute peak responsivity of the detector is small, up to about $V_B = -0.5 \text{ V}$. Beyond that it increases nearly linearly with bias reaching $R_p = 380 \text{ mA/W}$ at $V_B = -5 \text{ V}$. This type of behavior of responsivity versus bias is typical for a bound-to-quasibound QWIP. The peak quantum efficiency was 6.9% at bias $V_B = -1 \text{ V}$ for a 45° double pass. The lower quantum efficiency is due to the lower well doping density ($5 \times 10^{17} \text{ cm}^{-3}$) as it is necessary to suppress the dark current at the highest possible operating temperature.

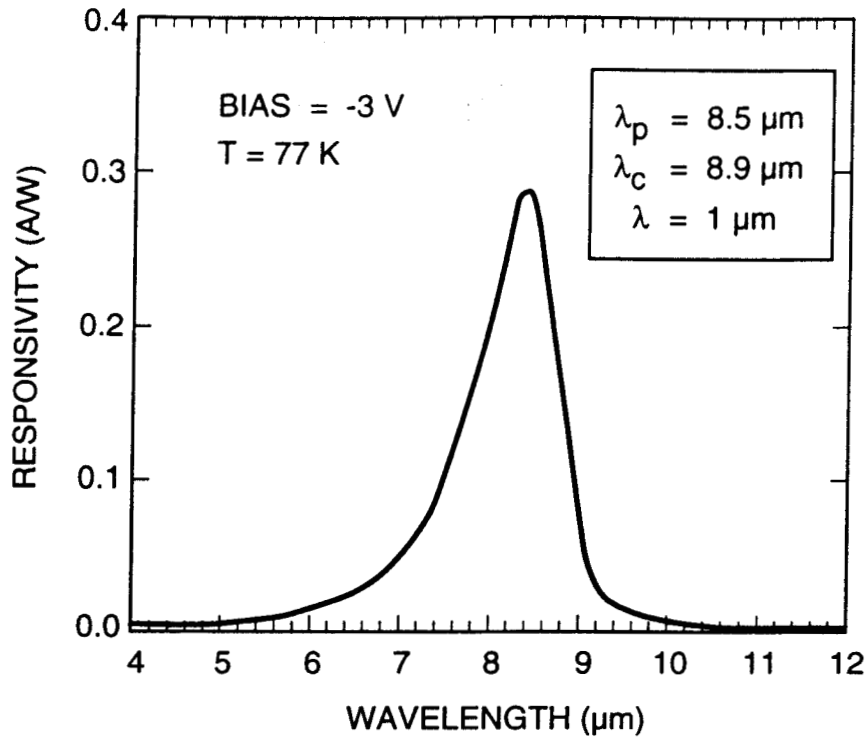


Fig. 3. Responsivity spectrum of a bound-to-quasibound LWIR QWIP test structure at temperature $T = 77$ K. The spectral response peak is at $8.4 \mu\text{m}$ and the long wavelength cutoff is at $8.9 \mu\text{m}$.

4. 14-15 MICRON 128X128 QWIP IMAGING CAMERA

It is well known that QWIPs do not absorb radiation incident normal to the surface unless the IR radiation have an electric field component normal to the layers of superlattice (growth direction)³. As we have discussed before³ many more passes of IR light inside the detector structure can be obtained by incorporating a randomly roughened reflecting surface on top of the detectors which also removes the light coupling limitations and makes two dimensional QWIP imaging arrays feasible. The photoconductive QWIPs of the 128x128 FPAs were then fabricated by wet chemical etching through the photosensitive GaAs/Al_xGa_{1-x}As multi quantum well layers into the 0.5 μm thick doped GaAs contact layer. The pitch of the FPA is 50 μm and the actual pixel size is 38x38 μm². Then the random reflectors on the top of the detectors were covered with Au/Ge and Au for Ohmic contact and reflection. Then indium bumps were evaporated on top of the detectors for Si read out circuit (ROC) hybridization. A

single QWIP FPA was chosen (cutoff wavelength of this sample is $14.9\text{ }\mu\text{m}$) and bonded to a 128×128 Si multiplexer (Amber AE-159) and biased at $V_b = -2.7\text{ V}$. The FPA was back-illuminated through the flat thinned substrate (thickness $\approx 25\text{ }\mu\text{m}$). This initial array gave excellent images with 99.9% of the pixels working, demonstrating the high yield of GaAs technology. Excellent uncorrected photocurrent uniformity (pixel-to-pixel) of the 16384 pixels of the 128×128 FPA is achieved with a standard deviation of only $\sigma=2.4\%$.⁴ The residual non-uniformity after correction was 0.05% and it is excellent compared to other types of focal plane arrays in the same wavelength region.

5. 8-9 MICRON 256X256 QWIP HAND-HELD CAMERA

After the random reflector array was defined by the lithography and dry etching, the photoconductive QWIPs of the 256×256 FPAs were fabricated by wet chemical etching through the photosensitive GaAs/ $\text{Al}_x\text{Ga}_{1-x}\text{As}$ multi-quantum well layers into the $0.5\text{ }\mu\text{m}$ thick doped GaAs bottom contact layer. The pitch of the FPA is $38\text{ }\mu\text{m}$ and the actual pixel size is $28\times 28\text{ }\mu\text{m}^2$. The random reflectors on top of the detectors were then covered with Au/Ge and Au for Ohmic contact and reflection. A single QWIP FPA was chosen and hybridized (via indium bump-bonding process) to a 256×256 CMOS multiplexer (Amber AE-166) and biased at $V_B = -1.0\text{ V}$. The FPA was back-illuminated through the flat thinned substrate membrane (thickness $\approx 1300\text{ }\text{\AA}$). This initial array gave excellent images with 99.98% of the pixels working (number of dead pixels ≈ 10), demonstrating the high yield of GaAs technology. The measured NE ΔT of the FPA at an operating temperature of $T = 70\text{ K}$, bias $V_B = -1\text{ V}$ for 300 K background and the mean value is 26 mK . This agrees reasonably with our estimated value of 8 mK based on test structure data. The peak quantum efficiency of the FPA was 3.3% (lower focal plane array quantum efficiency is attributed to 54% fill factor and 90% charge injection efficiency) and this corresponds to an average of three passes of IR radiation (equivalent to a single 45° pass) through the photosensitive multi-quantum well region.

A 256x256 QWIP FPA hybrid was mounted onto a 250 mW integral Sterling closed-cycle cooler assembly and installed into an Amber RADIANCE 1™ camera-body, to demonstrate a hand-held LWIR camera (shown in Fig. 4). The camera is equipped with a 32-bit floating-point digital signal processor combined with multi-tasking software, providing the speed and power to execute complex image-processing and analysis functions inside the camera body itself. The other element of the camera is a 100 mm focal length germanium lens, with a 5.5 degree field of view. It is designed to be transparent in the 8-12 μm wavelength range, to be compatible with the QWIP's 8.5 μm operation. The digital acquisition resolution of the camera is 12-bits, which determines the instantaneous dynamic range of the camera (i.e., 4096). However, the dynamic range of QWIP is 85 Decibels. Its nominal power consumption is less than 50 Watts ⁵.

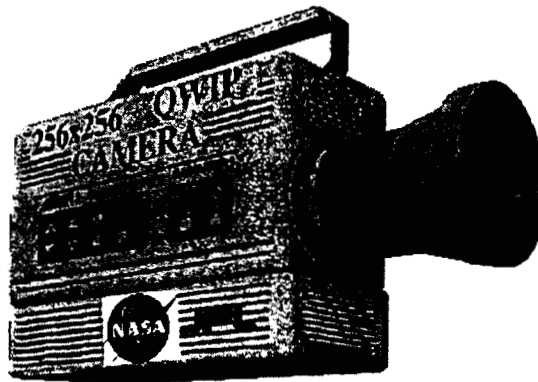


Fig. 4 Picture of the first 256x256 hand-held LWIR camera equipped with 256x256 QWIP FPA (QWIP RADIANCE™).

6. 8-9 MICRON 640X486 QWIP IMAGING CAMERA

Although random reflectors have achieved relatively high quantum efficiencies with large test device structures, it is not possible to achieve the similar high quantum efficiencies with random reflectors on small focal plane array pixels due to the reduced width-to-height aspect ratios. In addition, it is difficult to fabricate random reflectors for shorter wavelength detectors relative to very long-wavelength detectors (i.e., 15 μm) due to the fact that feature sizes of random reflectors are linearly proportional to the peak wavelength of QWIPs. As we have discussed before ³, more IR light can be coupled to the QWIP

detector structure by incorporating a two dimensional grating surface on top of the detectors which also removes the light coupling limitations and makes two dimensional QWIP imaging arrays feasible.

After the 2-D grating array was defined by the photolithography and dry etching, the photoconductive QWIPs of the 640x486 FPAs were fabricated by wet chemical etching through the photosensitive GaAs/Al_xGa_{1-x}As multi-quantum well layers into the 0.5 μm thick doped GaAs bottom contact layer. The pitch of the FPA is 25 μm and the actual pixel size is 18x18 μm^2 . The cross gratings on top of the detectors were then covered with Au/Ge and Au for Ohmic contact and reflection. A single QWIP FPA was chosen and hybridized to a 640x486 direct injection silicon readout multiplexer (Amber AE-181) and biased at $V_B = -2.0$ V. The FPA was back-illuminated through the flat thinned substrate membrane (thickness ≈ 1300 Å). This thinned GaAs FPA membrane has completely eliminated the thermal mismatch between the silicon CMOS readout multiplexer and the GaAs based QWIP FPA. Basically, the thinned GaAs based QWIP FPA membrane adapts to the thermal expansion and contraction coefficients of the silicon readout multiplexer. Therefore, this thinning has played an extremely important role in the fabrication of large area FPA hybrids. In addition, this thinning has completely eliminated the pixel-to-pixel optical cross-talk of the FPA. This initial array gave excellent images with 99.9% of the pixels working, demonstrating the high yield of GaAs technology. Figure 5 shows the experimentally measured NE ΔT of the FPA at an operating temperature of $T = 70$ K, bias $V_B = -2$ V at 300 K background and the mean value 36 mK. This agrees reasonably with our estimated value of 25 mK based on test structure data. The experimentally measured peak quantum efficiency of the FPA was 2.3% (lower focal plane array quantum efficiency is attributed to 51% fill factor and 30% reflection loss from the GaAs back surface). Therefore, the corrected quantum efficiency of a focal plane detectors is 6.5% and this corresponds to an average of two pass of IR radiation (equivalent to a single 45° pass) through the photosensitive multi-quantum well region.

A 640X486 QWIP FPA hybrid was mounted onto a 84-pin lead-less chip carrier and installed into a laboratory dewar which is cooled by liquid nitrogen to demonstrate a LWIR imaging camera). The other

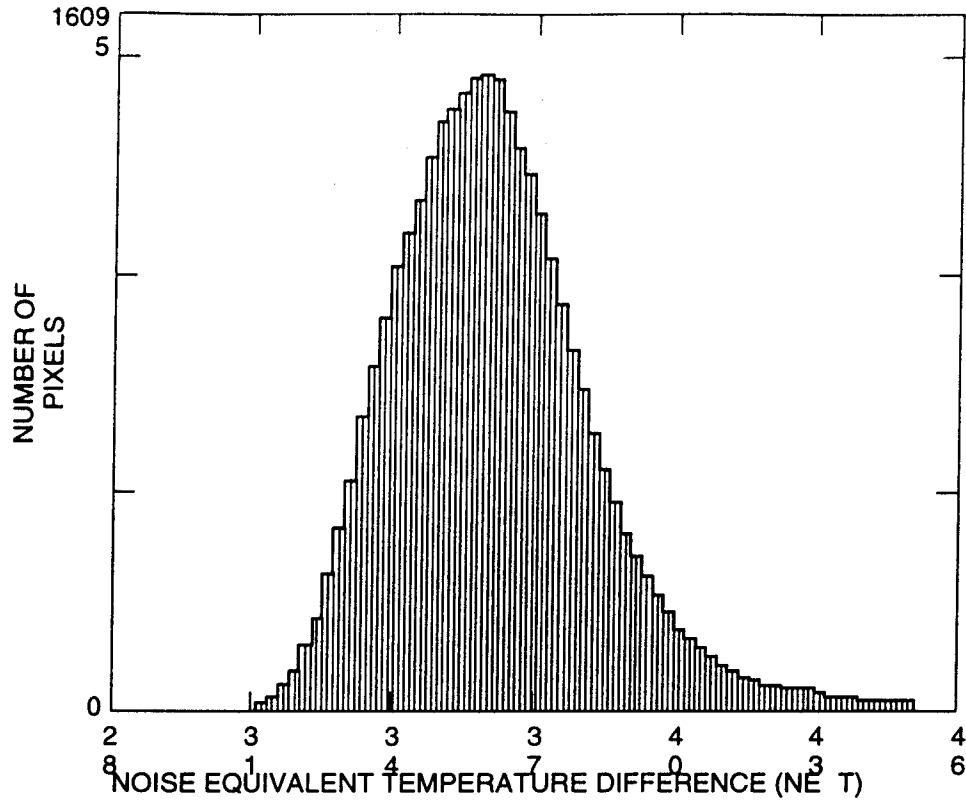


Fig. 5. Noise equivalent temperature difference (NEAT) histogram of the 311,040 pixels of the 640 x 486 array showing a high uniformity of the FPA. The uncorrected non-uniformity (= standard deviation/mean) of this unoptimized FPA is only 5.6% including 1% non-uniformity of ROC and 1.4% non-uniformity due to the cold-stop not being able to give the same field of view to all the pixels in the FPA.

element of the camera is a 100 mm focal length AR coated germanium lens, which gives a $9.2^\circ \times 6.9^\circ$ field of view. The measured mean NEAT of the QWIP camera is 36 mK at an operating temperature of $T = 70$ K and bias $V_B = -2$ V at 300 K background. The uncorrected NEAT non-uniformity of the 640x486 FPA is about 5.6% (= σ / mean).

Video images were taken at a frame rate of 30 Hz at temperatures as high as $T = 70$ K using a ROC capacitor having a charge capacity of 9×10^6 electrons. The non-uniformity after two-point (17° and 27° Celsius) correction improves to an impressive 0.1%. Figure 6 shows a frame of video image taken with this long-wavelength 640x486 QWIP camera. This image demonstrates the high sensitivity of the

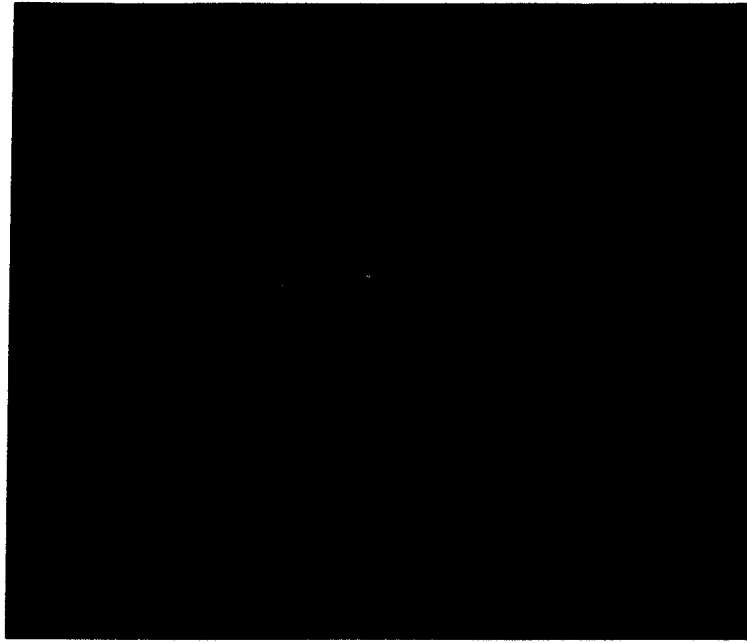


Fig. 6. This picture was taken in the night (around midnight) and it clearly shows where automobiles were parked during the day time. This image demonstrates the high sensitivity of the 640 x 486 long-wavelength QWIP staring array camera.

640 x 486 long-wavelength QWIP staring array camera. As mentioned earlier, this high yield is due to the excellent GaAs growth uniformity and the mature GaAs processing technology.

7. BROAD-BAND QWIP

A broad-band MQW structure can be designed by repeating a unit of several quantum wells with slightly different parameters such as well width and barrier height. The device structure involved 33 repeated layers of GaAs three-quantum-well units separated by $L_B \sim 575 \text{ \AA}$ thick $\text{Al}_x\text{Ga}_{1-x}\text{As}$ barriers⁶. The well thickness of the quantum wells of three-quantum-well units are designed to respond at peak wavelengths around 13, 14, and 15 μm respectively. These wells are separated by $L_u \sim 75 \text{ \AA}$ thick $\text{Al}_x\text{Ga}_{1-x}\text{As}$ barriers. The Al mole fraction (x) of barriers throughout the structure was chosen such that the $\lambda_p = 13 \mu\text{m}$ quantum well operates under bound-to-quasibound conditions. The excited state energy level broadening has further enhanced due to overlap of the wavefunctions associated with excited states

of quantum wells separated by thin barriers. Energy band calculations based on a two band model shows excited state energy levels spreading about 28 meV. The responsivity spectra of these detectors were measured using a 1000 K blackbody source and a grating monochromator. The detectors were back illuminated through a 45° polished facet to obtain normalized responsivity spectra at different bias voltages. Then the absolute spectral responsivities were obtained by measuring total photocurrent due to a calibrated black-body source. In Fig. 7, responsivity curve at $V_B = -3$ V bias voltage shows broadening of the spectral response up to $\Delta\lambda \sim 5.5 \mu\text{m}$, i.e. the full width at half maximum from 10.5 - 16 μm . This broadening $\Delta\lambda/\lambda_p \sim 42\%$ is about a 400 % increase compared to a typical bound-to-quasibound QWIP.

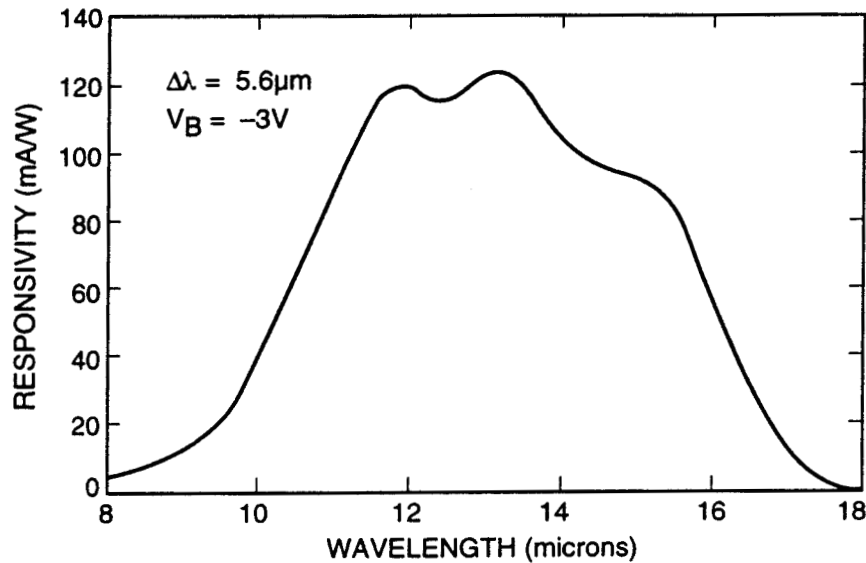


Fig. 7. Experimentally measured responsivity spectrum of broadband QWIP at bias voltage $V_B = -3$ V.

8. DUALBAND (MID-WAVELENGTH AND LONG-WAVELENGTH) DETECTORS

There are several applications such as target recognition and discrimination which require monolithic mid and long wavelength dualband large area, uniform, reproducible, low cost and low 1/f noise infrared FPAs. For example, a dualband FPA camera would provide the absolute temperature of the target which is extremely important to the process of identifying temperature difference between targets, war heads and decoys. The GaAs based QWIP is a potential candidate for development of such a two-color FPAs.

Until recently, the most developed and discussed two-color QWIP detector was the voltage tunable two stack QWIP. This device structure consists of two QWIP structures, one tuned for mid-wavelength detection and the other stack tuned for long-wavelength detection. This device structure utilizes the advantage of formation of electric field domains to select the response of one or the other detector^{7,8} (MQW region). The difficulties associated with this type of two-color QWIP FPA are that these detectors need two different voltages to operate and long-wavelength sensitive segment of the device needs very high bias voltage (> 8 V) to switch on the long-wavelength infrared (LWIR) detection. The other disadvantage is the voltage tunable scheme will not provide simultaneous data from both wavelength bands.

Therefore, we have developed a following QWIP device structure which can be processed in to dualband QWIP FPAs with dual or triple contacts to access the CMOS readout multiplexer^{9,10}. The device structure consists of a stack of 30 periods of mid-wavelength infrared (MWIR) QWIP structure and another stack of 10 periods of LWIR QWIP structure separated by a heavily doped 0.5 μm thick intermediate GaAs contact layer. The first stack (LWIR) consist of 10 periods of 500 Å $\text{Al}_x\text{Ga}_{1-x}\text{As}$ barrier and a GaAs well. This LWIR QWIP structure has been designed to have a bound-to-quasibound intersubband absorption peak at 8.5 μm , since the dark current of the device structure is expected to dominate by the longer wavelength portion of the device structure. The second stack (MWIR) consist of 30 periods of 500 Å $\text{Al}_x\text{Ga}_{1-x}\text{As}$ barrier and narrow $\text{In}_x\text{Ga}_{1-x}\text{As}$ well sandwiched between two thin layers of GaAs. This MWIR QWIP structure has been designed to have a bound-to-continuum intersubband absorption peak at 4.2 μm , since photo current and dark current of the MWIR device structure is relatively small compared to the LWIR portion of the device structure. This two-color QWIP structure is then sandwiched between 0.5 μm GaAs top and bottom contact layers doped $n = 5 \times 10^{17} \text{ cm}^{-3}$, and has been grown on a semi-insulating GaAs substrate by MBE. Then a 1.0 μm thick GaAs cap layer on top of a 300 Å $\text{Al}_{0.3}\text{Ga}_{0.7}\text{As}$ stop-etch layer has to be grown in situ on top of the device structure to fabricate the light coupling optical cavity.

The detectors were back illuminated through a 45° polished facet as described earlier and a simultaneously measured responsivity spectrum of vertically integrated dualband QWIP is shown in Fig. 8. The responsivity of the MWIR detector peaks at 4.4 μm and the peak responsivity (R_p) of the detector is 140 mA/W at bias $V_B = -3$ V. The spectral width and the cutoff wavelength of the MWIR detector are $\Delta\lambda/\lambda = 20\%$ and $\lambda_c = 5$ μm respectively. The responsivity of the LWIR detector peaks at 8.8 μm and the peak responsivity (R_p) of the detector is 150 mA/W at bias $V_B = -1.2$ V. The spectral width and the cutoff wavelength of the LWIR detector are $\Delta\lambda/\lambda = 14\%$ and $\lambda_c = 9.4$ μm respectively. The measured absolute peak responsivity of both MWIR and LWIR detectors are small, up to about $V_B = -0.5$ V. Beyond that it increase nearly linearly with bias in both MWIR and LWIR detectors reaching $R_p = 210$ and 440 mA/W respectively at $V_B = -4$ V. This type of behavior of responsivity versus bias is typical for a bound-to-continuum and bound-to-quasibound QWIPs in MWIR and LWIR bands respectively. The peak quantum efficiency of MWIR and LWIR detectors were 2.6% and 16.4% respectively.

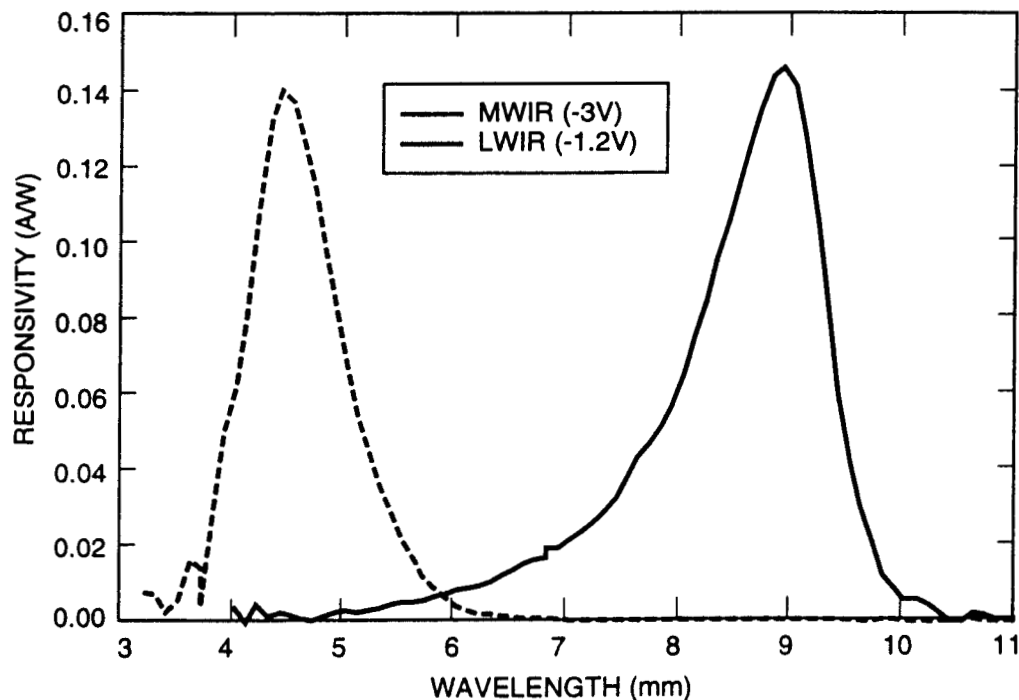


Fig. 8. Simultaneously measured responsivity spectrum of vertically integrated MWIR and LWIR dualband QWIP detector.

detector peaks at $8.8 \mu\text{m}$ and the peak responsivity (R_p) of the detector is 150 mA/W at bias $V_B = -1.2 \text{ V}$. The spectral width and the cutoff wavelength of the LWIR detector are $\Delta\lambda/\lambda = 14\%$ and $\lambda_c = 9.4 \mu\text{m}$ respectively. The measured absolute peak responsivity of both MWIR and LWIR detectors are small, up to about $V_B = -0.5 \text{ V}$. Beyond that it increase nearly linearly with bias in both MWIR and LWIR detectors reaching $R_p = 210$ and 440 mA/W respectively at $V_B = -4 \text{ V}$. This type of behavior of responsivity versus bias is typical for a bound-to-continuum and bound-to-quasibound QWIPs in MWIR and LWIR bands respectively. The peak quantum efficiency of MWIR and LWIR detectors were 2.6% and 16.4% respectively at operating biases indicated in Fig. 8 for a 45° double pass. The lower quantum efficiency of MWIR detector is due to the lower well doping density ($5 \times 10^{17} \text{ cm}^{-3}$). The peak detectivities of both MWIR and LWIR detectors were estimated at different operating temperature and bias voltages using experimentally measured noise currents and results are shown in Figs. 9 and 10.

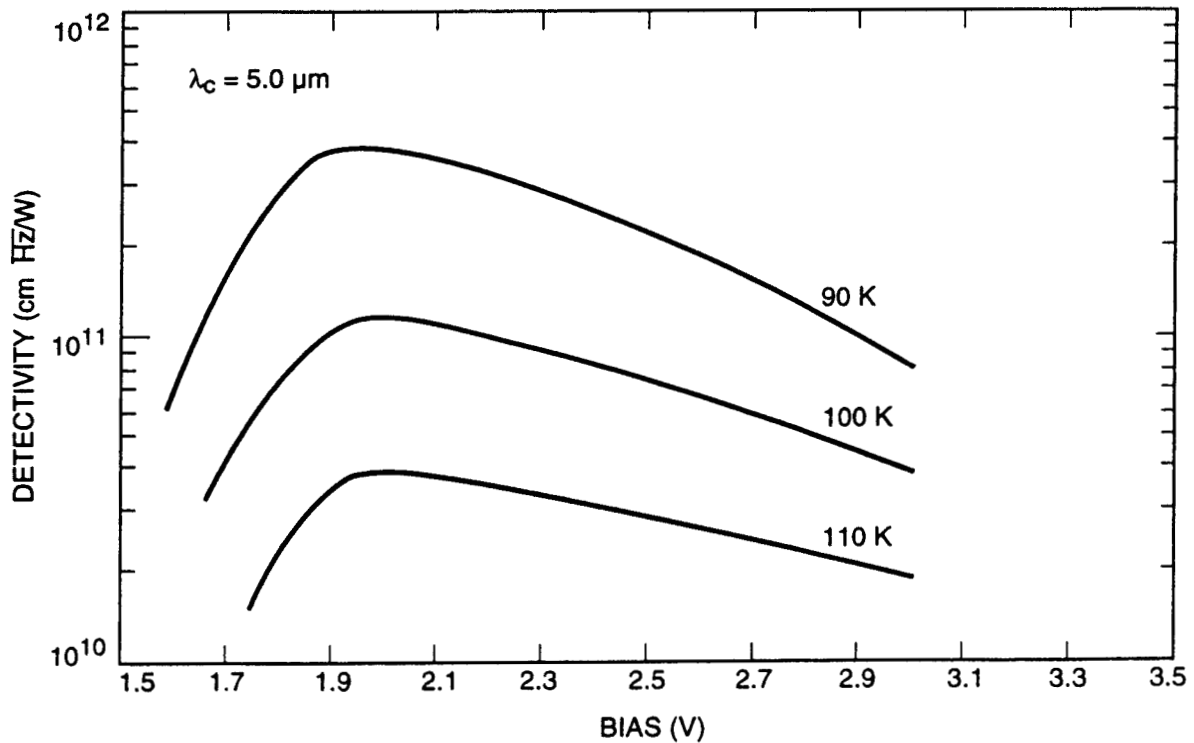


Fig. 9. Experimentally measured peak detectivity of MWIR detector as a function of bias voltage at three different operating temperatures.

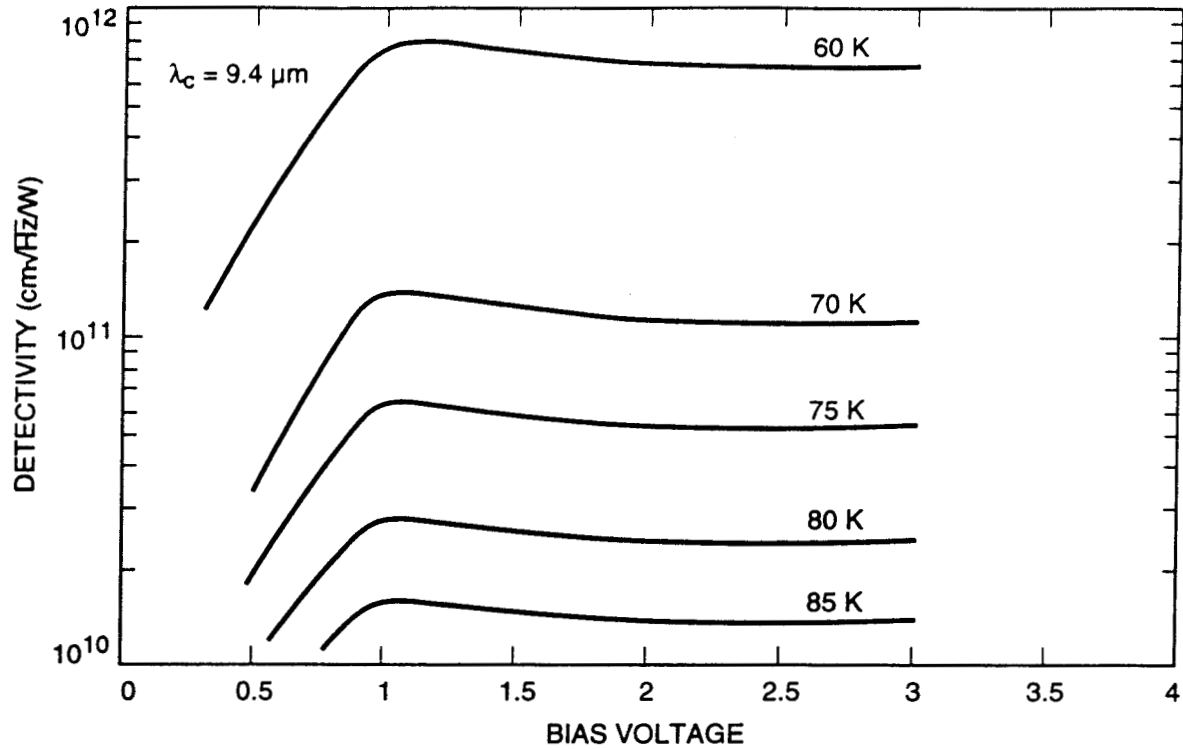


Fig. 10. Experimentally measured peak detectivity of LWIR detector as a function of bias voltage at five different operating temperatures.

9. DUALBAND (LONG-WAVELENGTH AND VERY LONG-WAVELENGTH) DETECTORS

As we discussed in the previous section of this paper, there are many target recognition and discrimination applications which require monolithic dualband large area, uniform, reproducible, low cost and low 1/f noise infrared FPAs. The general notion is that dualband target recognition and discrimination capability significantly improve with increasing wavelength separation between the two wavelength bands in consideration. Therefore, we are currently developing a 640x486 LWIR and very-long-wavelength infrared (VWIR) dualband QWIP FPA camera. Thus, we have developed a following QWIP device structure which can be processed in to dualband QWIP FPAs with dual or triple contacts to access the CMOS readout multiplexer. Single indium bump per pixel is usable only in the case of interlace readout scheme (i.e., odd rows for one color and the even rows for the other color) which uses an existing single color CMOS readout multiplexer. The advantages of this scheme are that it provides

simultaneous data readout and allows to use currently available single color CMOS readout multiplexers. However, the disadvantage is that it does not provides a full fill factor for both wavelength bands. This problem can be eliminated by fabricating $(n+1)$ terminals (e.g., three terminals for dualband) per pixel and hybridizing with a multicolor readout having n readout cells per detector pitch, where n is the number of bands.

The device structure consists of a stack of 25 periods of LWIR QWIP structure and another stack of 25 periods of VWIR QWIP structure separated by a heavily doped 0.5 μm thick intermediate GaAs contact layer. The first stack (VWIR) consist of 25 periods of 500 Å $\text{Al}_x\text{Ga}_{1-x}\text{As}$ barrier and a GaAs well. This VWIR QWIP structure has been designed to have a bound-to-quasibound intersubband absorption peak at 15 μm , since the dark current of the device structure is expected to dominate by the longer wavelength portion of the device structure. The second stack (LWIR) consist of 25 periods of 500 Å $\text{Al}_x\text{Ga}_{1-x}\text{As}$ barrier and narrow GaAs well. This LWIR QWIP structure has been designed to have a bound-to-continuum intersubband absorption peak at 8.5 μm , since photo current and dark current of the MWIR device structure is relatively small compared to the VWIR portion of the device structure. This whole dualband QWIP structure is then sandwiched between 0.5 μm GaAs top and bottom contact layers doped $n = 5 \times 10^{17} \text{ cm}^{-3}$, and has grown on a semi-insulating GaAs substrate by MBE. Then a 1.0 μm thick GaAs cap layer on top of a 300 Å $\text{Al}_{0.3}\text{Ga}_{0.7}\text{As}$ stop-etch layer has to be grown in situ on top of the device structure for the fabrication of light coupling optical cavity.

The detectors were back illuminated through a 45° polished facet as described earlier and a simultaneously measured responsivity spectrum of vertically integrated dualband QWIP is shown in Fig. 11. The responsivity of the LWIR detector peaks at 8.3 μm and the peak responsivity (R_p) of the detector is 260 mA/W at bias $V_B = -2.5 \text{ V}$. The spectral width and the cutoff wavelength of the LWIR detector are $\Delta\lambda/\lambda = 19\%$ and $\lambda_c = 9.3 \mu\text{m}$ respectively. The responsivity of the VWIR detector peaks at 15.2 μm and the peak responsivity (R_p) of the detector is 340 mA/W at bias $V_B = -2.0 \text{ V}$. The spectral width and the cutoff wavelength of the LWIR detector are $\Delta\lambda/\lambda = 12\%$ and $\lambda_c = 15.9 \mu\text{m}$ respectively. The measured absolute peak responsivity of both LWIR and VWIR detectors are small, up to about

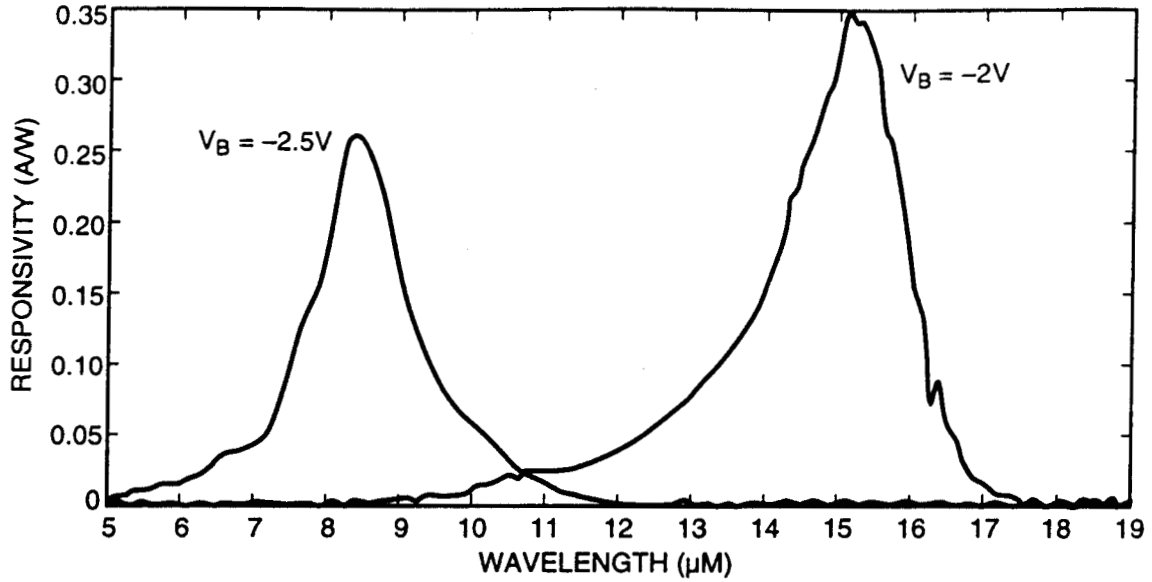


Fig. 11. Simultaneously measured responsivity spectrum of vertically integrated LWIR and VWIR dualband QWIP detector.

$V_B = -0.5$ V. Beyond that it increase nearly linearly with bias in both LWIR and VWIR detectors reaching $R_p = 0.3$ (at $V_B = -2V$) and 1 A/W (at $V_B = -3V$) respectively. This type of behavior of responsivity versus bias is typical for bound-to-continuum and bound-to-quasibound QWIPs in LWIR and VWIR bands respectively. The peak quantum efficiency of LWIR and VWIR detectors were 2.6% and 16.4% respectively at operating biases indicated in Fig. 11 for a 45° double pass. The lower quantum efficiency of LWIR detector is due to the lower well doping density ($5 \times 10^{17} \text{ cm}^{-3}$). The peak detectivities of both LWIR and VWIR detectors were estimated at different operating temperature and bias voltages using experimentally measured noise currents and results are shown in Figs. 12 and 13.

10. HIGH PERFORMANCE QWIPS FOR LOW BACKGROUND APPLICATIONS

In this section, we discuss the demonstration of high performance QWIPs for low background applications. Improving QWIP performance depends largely on minimizing the Shott noise of the dark current (the current that flows through a biased detector in the dark, i.e., with no photons impinging on it) and improving the quantum efficiency. In order to analyze the dark current of a QWIP which has a

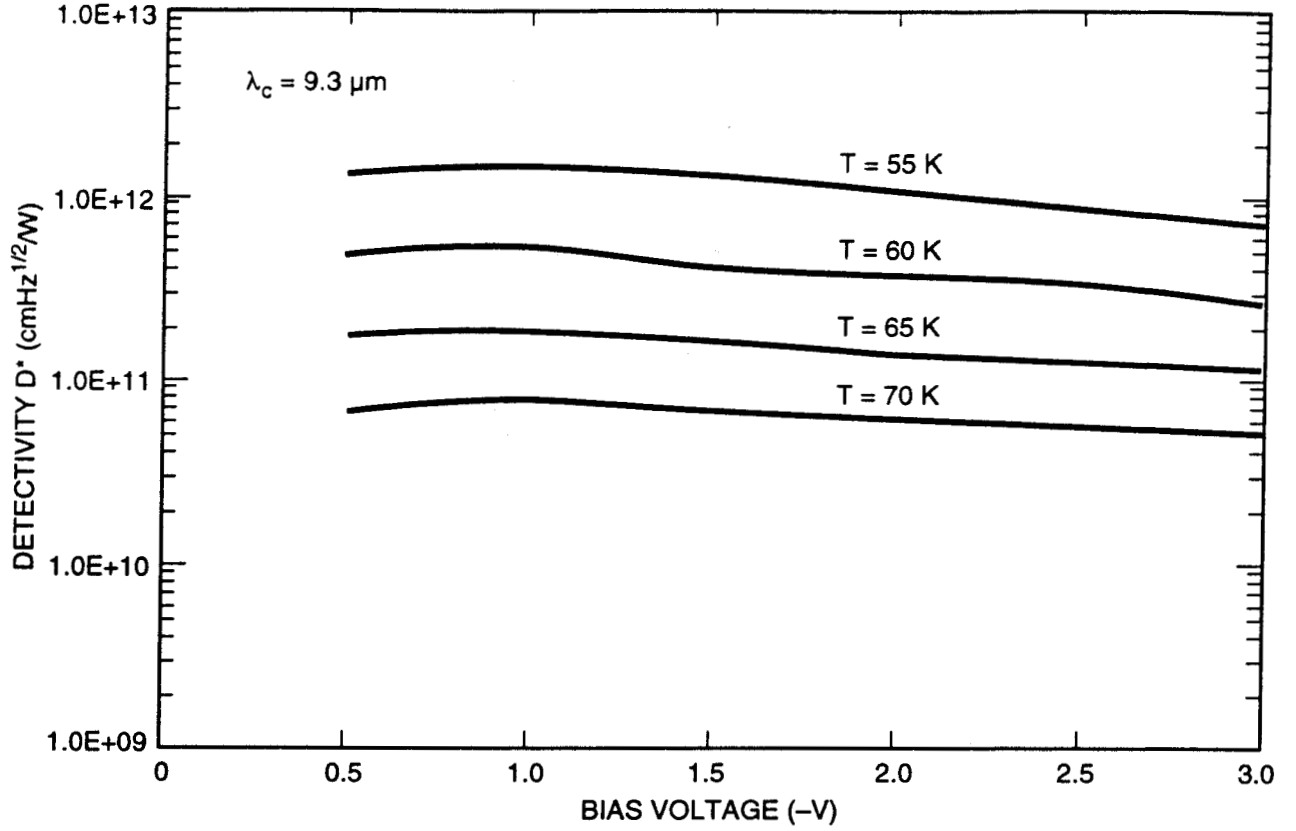


Fig. 12. Experimentally measured peak detectivity of LWIR detector as a function of bias voltage at three different operating temperatures.

intersubband absorption peak in long-wavelength region, we first calculated the effective number of electrons^{3,11} $n(V)$ which are thermally excited into the continuum transport states, as a function of bias voltage V , using the following expression.

$$n(V) = \left(\frac{m^*}{\pi \hbar^2 L_p} \right) \int_{E_0}^{\infty} f(E) T(E, V) dE \quad (1)$$

The first factor containing the effective mass m^* represents the average three dimensional density of states. Where L_p is the superlattice period, $f(E)$ is the Fermi factor $f(E) = [1 + \exp(E - E_0 - E_F)/KT]^{-1}$, E_0 is the bound state energy, E_F is the two-dimensional Fermi energy, E is the energy of the electron, and $T(E, V)$ is the tunneling current transmission factor which is obtained by using WKB approximation to a biased quantum well. In equation 1, the effective number of electrons above the barrier account for thermionic contribution and the number of electrons below the barrier account for thermionic assisted

photons impinging on it). As we have discussed elsewhere¹, at temperatures above 45 K, the dark current of the QWIP is entirely dominated by classic thermionic emission of ground state electrons directly out of the well into the energy continuum. Minimizing this last component is critical to the commercial success of the QWIP as it allows the highly-desirable high-temperature camera operation. Therefore, we have designed the *bound-to-quasibound* quantum well by placing the first excited state exactly at the well top as shown in Fig. 1. The best previous QWIPs (pioneered by Barry Levine *et al.* at AT&T Bell Labs) were of the bound-to-continuum variety, so-called because the first excited state was a continuum energy band above the well top (typically 10 meV). Dropping the first excited state to the well top causes the barrier to thermionic emission (roughly the energy height from the ground state to the well top) to be ~ 10 meV more in our bound-to-quasibound QWIP than in the bound-to-continuum one, theoretically causing the dark current to drop by a factor of ~ 6 at a temperature of 70 K³.

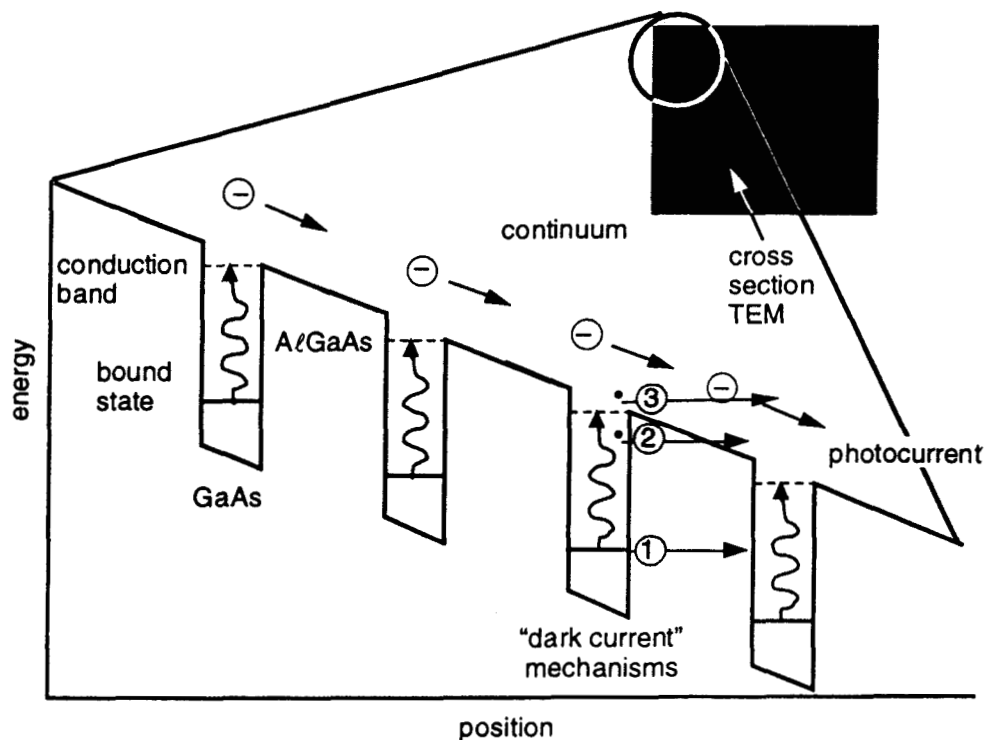


Fig. 1. Schematic diagram of the conduction band in a bound-to-quasibound QWIP in an externally applied electric field. Absorption of IR photons can photoexcite electrons from the ground state of the quantum well into the continuum, causing a photocurrent. Three dark current mechanisms are also shown: ground state tunneling (1); thermally assisted tunneling (2); and thermionic emission (3). The inset shows a cross-section transmission electron micrograph of a QWIP sample.

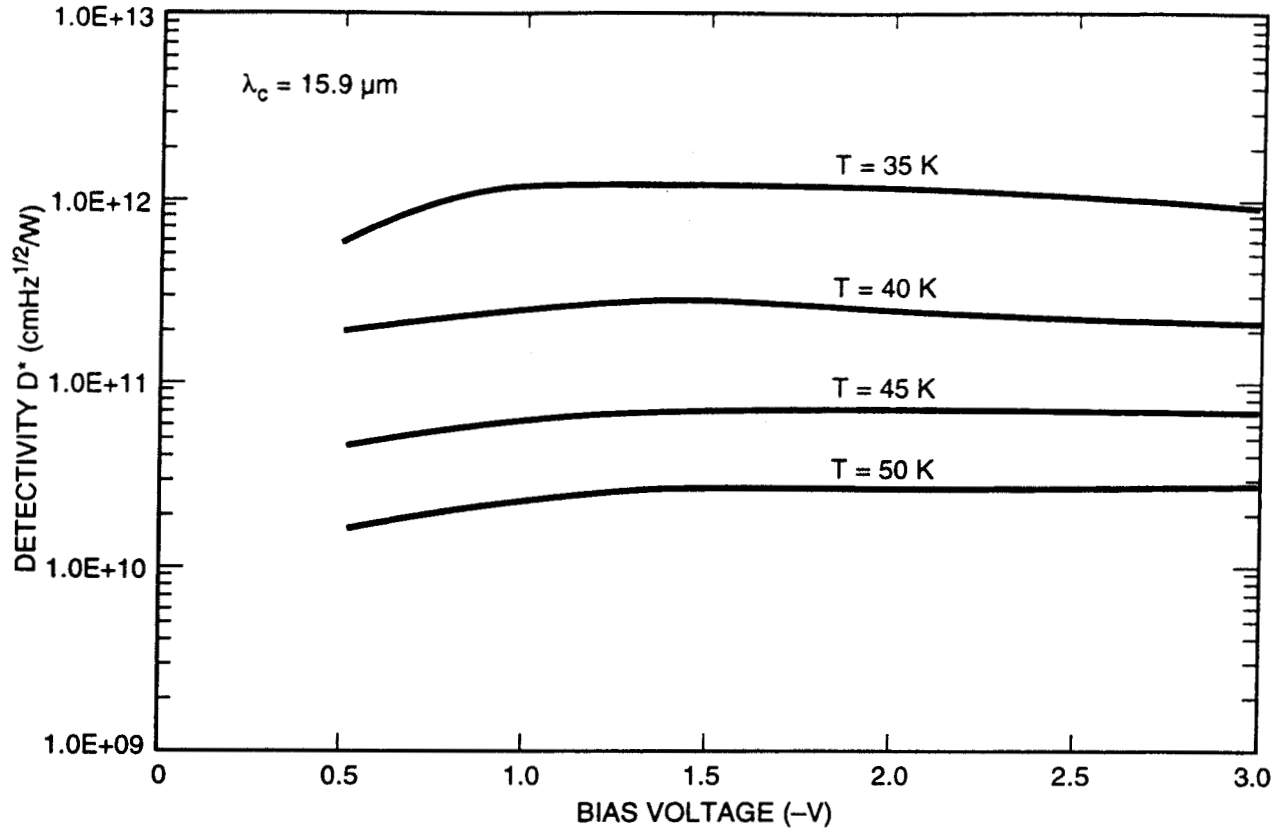


Fig. 13. Experimentally measured peak detectivity of VWIR detector as a function of bias voltage at five different operating temperatures.

tunneling and tunneling contribution of the dark current. Then the bias-dependent dark current $I_d(V)$ was calculated, using $I_d(V) = eAn(V)v(V)$, where $v(V)$ is the average transport velocity, A is the device area, and e is the electronic charge. The average transport velocity was calculated using $v(V) = \mu F [1 + (\mu F/v_s)^2]^{-1/2}$, where μ is the mobility, F is the electric field, and v_s is the saturated drift velocity. In order to obtain bias-dependent dark current at $T = 60K$, $\mu = 1200 \text{ cm}^2/Vs$ and $v_s = 5.5 \times 10^6 \text{ cm/s}$ was used. Fig. 14 shows the $T = 60K$ dark current due to thermionic emission, total dark current (thermionic + thermionic assisted tunneling + tunneling), and experimental dark current of a QWIP sample which has cutoff wavelength $\lambda_c = 10 \text{ } \mu\text{m}$. According to the calculations tunneling through the barriers dominates the dark current at temperatures below 30K, and at temperatures above 30 K thermionic emission into the continuum transport states dominates the dark current.

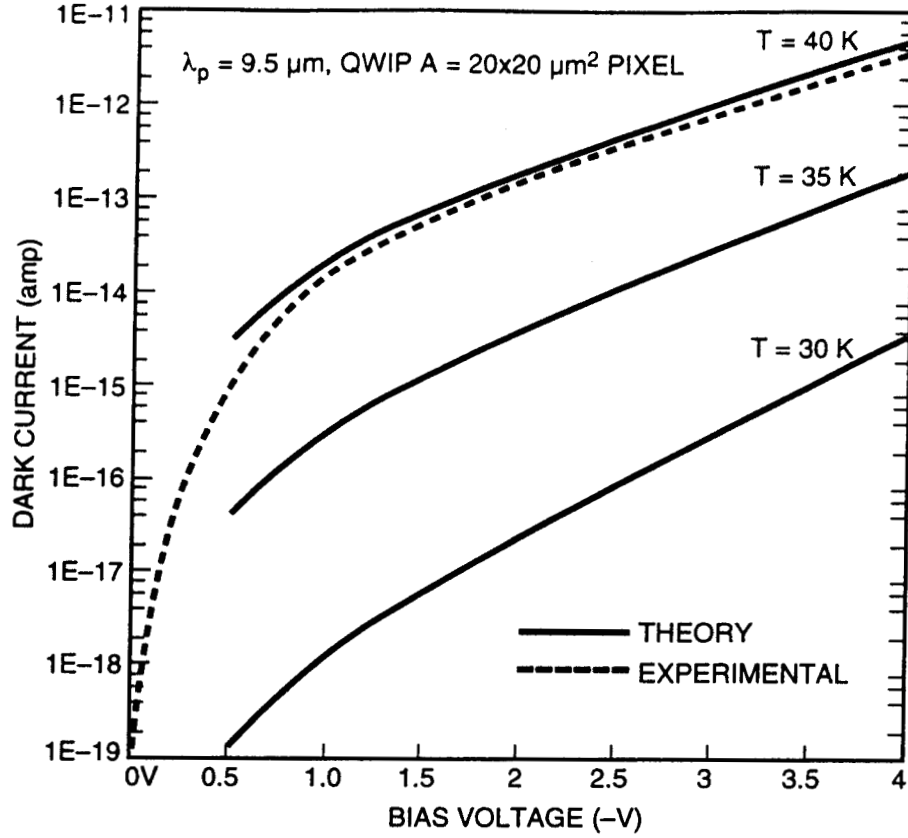


Fig. 14. Comparison of experimental (solid curves) and theoretical (dashed) dark current versus bias voltage curves at various temperatures for a 10 μm cutoff QWIP.

Eight n-type doped QWIP device structures were grown for this experiment. These n-doped QWIPs were grown using molecular beam epitaxy and the wells and contact layers were doped with Si. The quantum well widths L_w range from 35 to 50 Å, while the barrier widths are approximately constant at $L_b = 500$ Å. The Al molar fraction in the $\text{Al}_x\text{Ga}_{1-x}\text{As}$ barriers varies from $x = 0.24$ to 0.30 (corresponding to cutoff wavelengths of $\lambda_c = 8.3 - 10.3$ μm). The photosensitive doped multiquantum-well (MQW) region (containing 25 to 50 periods) is sandwiched between similarly doped top (0.5 μm) and bottom (0.5 μm) ohmic contact layers. These structural parameters have been chosen to give a very wide variation in the QWIP absorption and transport properties. All eight QWIP samples are n-doped with intersubband infrared transition occurring between a single localized bound state in the well and a delocalized state in the continuum. Thus, the intersubband transition occurs from the bound state to a

delocalized state in the continuum. In the presence of an electric field, the photoexcited carrier can be effectively swept out of the quantum well region.

All eight QWIP samples were processed into 200 μm diameter mesas (area = $3.14 \times 10^{-4} \text{ cm}^2$) using wet chemical etching and Au/Ge ohmic contacts were evaporated onto the top and bottom contact layers. The dark current versus voltage curves for all samples were measured as a function of temperature from $T = 40\text{-}70 \text{ K}$ and Fig. 14 shows the current-voltage curve of one sample. As expected, Fig. 1 clearly shows that the $T = 40 \text{ K}$ dark current of these QWIP devices are many orders of magnitude smaller than the dark current at $T = 70 \text{ K}$. This clearly indicates that the dark current of these devices are thermionic dominant down to 40 K and the tunneling induced dark current is insignificant.

The responsivity spectra of all detectors were measured using a 1000 K blackbody source and a grating monochromator. The detectors were back illuminated through a 45° polished facet and their normalized responsivity spectrums are shown in Fig. 15. The responsivities of all device structures peaked in the range from 7.7 μm and 9.7 μm . The peak responsivities (R_p), spectral widths ($\Delta\lambda$), cutoff wavelengths (λ_c) and quantum efficiency photoconductive gain products ($\eta \times g$) are listed in Table I. It is worth noting that hg product of sample four has increased to 17%. This is approximately a factor of 24 increase in hg product compared to hg product of our QWIP devices designed for high background and high temperature operation.

The current noise i_n was measured using a spectrum analyzer. The peak detectivity D^* can now be calculated from $D^* = R\sqrt{A\Delta f}/i_n$, where A is the area of the detector and $A = 27 \times 27 \mu\text{m}^2$. Table II shows the D^* values of both device structures at various bias voltages at $T = 40 \text{ K}$. These data clearly show that detectivities of 10 μm cutoff QWIPs reach mid $10^{13} \text{ cm}^2/\text{Hz}/\text{W}$ at $T = 40 \text{ K}$. As shown in Table II, these detectors are not showing background limited performance (BLIP) for moderately low background of $2 \times 10^9 \text{ photons}/\text{cm}^2/\text{sec}$ at $T = 40 \text{ K}$ operation. Since the dark current of these detectors are thermionically limited down to $T = 30 \text{ K}$, these detectors should demonstrated BLIP at $T = 35 \text{ K}$ for $2 \times 10^9 \text{ photons}/\text{cm}^2/\text{sec}$ background.

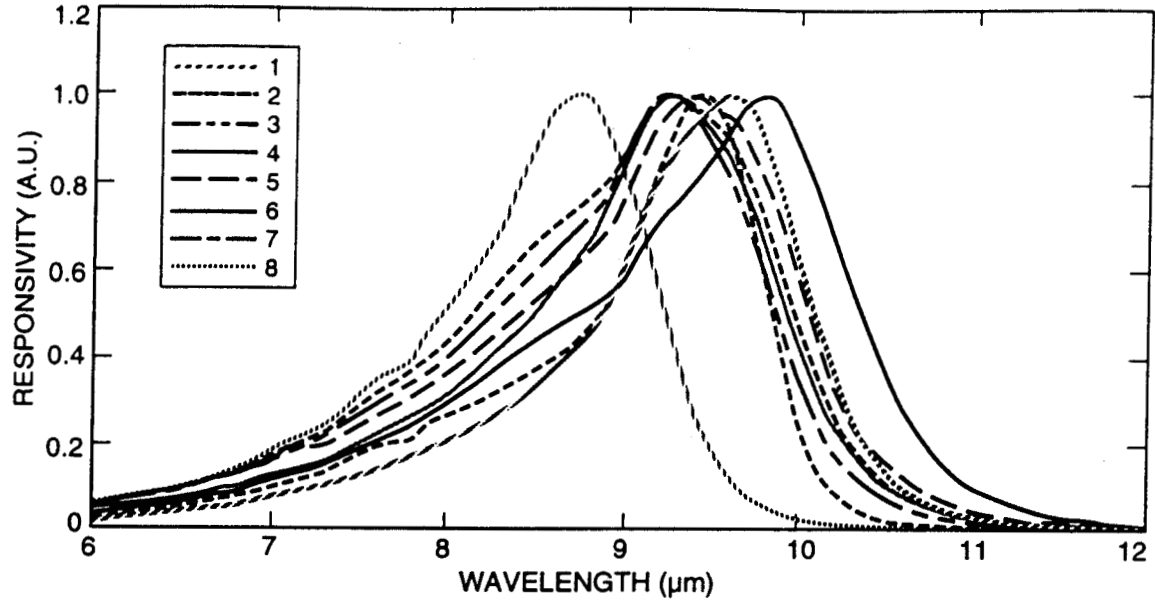


Fig. 15. Normalized responsivity spectra versus wavelength at $T=40$ K for all samples.

TABLE I. Responsivity spectral parameters of all eight samples.

Sample	Spectral Response (μm)			Device Performance (Detector Area $3.1 \times 10^{-4} \text{ cm}^2$)		
	λ_p	50% λ_c	$\Delta\lambda$	Peak R_p A/W @ 2V	Q.E. x Gain %	Dark Current @ 50K
1	9.6	10.1	1.1	0.65	8.4	1.1 E-11
2	9.4	10.1	1.6	0.61	8.0	8.0 E-11
3	9.3	9.8	1.6	0.38	5.2	2.0 E-11
4	9.3	9.8	1.2	1.26	17.0	9.0 E-11
5	9.4	10.0	1.8	0.46	6.1	1.0 E-10
6	9.7	10.3	1.5	0.54	5.3	3.0 E-10
7	8.5	8.9	1.0	0.15	2.2	1.0 E-12
8	7.7	8.3	1.3	0.34	5.5	2.5 E-12

11. APPLICATIONS

FIRE FIGHTING:

Video images were taken at a frame rate of 60 Hz at temperatures as high as $T = 70$ K, using a ROC capacitor having a charge capacity of 9×10^6 electrons (the maximum number of photoelectrons and dark electrons that can be counted in the time taken to read each detector pixel). This infrared camera helped a Los Angeles TV news crew get a unique perspective on fires that raced through the Southern California seaside community of Malibu in October, 1996. The camera was used on the station's news helicopter. This portable camera features infrared detectors which cover longer wavelengths than previous portable cameras could. This allows the camera to see through smoke and pinpoint lingering hotspots which are not normally visible. This enabled the TV station to transmit live images of hotspots in areas which appeared innocuous to the naked eye. These hotspots were a source of concern and difficult for firefighters, because they could flare up even after the fire appeared to have subsided. Figure 16 shows

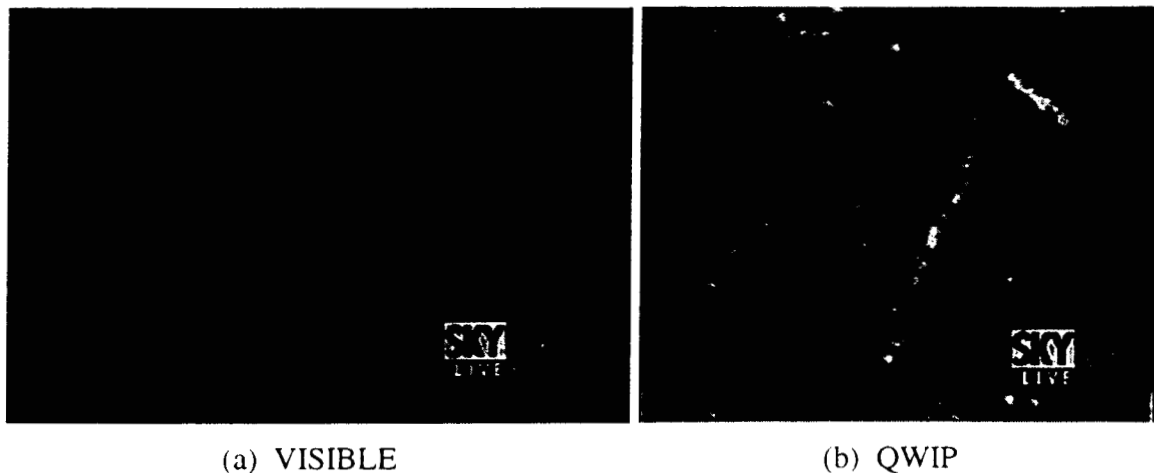


Fig. 16. Comparison of visible and infrared images of a just burned area as seen by a highly sensitive visible CCD camera and the long wavelength infrared camera in nighttime. (a) Visible image from a CCD camera. (b) Image from the 256x256 portable QWIP camera. This portable camera features infrared detectors covers longer wavelengths than previous portable cameras could. This allows the camera to see through smoke and pinpoint lingering hotspots which are not normally visible. This enables firefighters to locate the hotspots in areas which appeared innocuous to the naked eye. These hotspots are a source of concern and difficulty for firefighters, because fire can flare up even after it appears to have subsided. It works effectively in both daylight and nighttime conditions.

the comparison of visible and infrared images of a just burned area as seen by the news crew in nighttime. It works effectively in both daylight and nighttime conditions. The event marked the QWIP camera's debut as a fire observing device.

VOLCANOLOGY:

Recently, the camera has been used to observe volcanoes, mineral formations, weather and atmospheric conditions. This QWIP camera was taken to the Kilauea Volcano in, Hawaii. The objectives of this trip were to map geothermal features. The wide dynamic range enabled us to image volcanic features at temperatures much higher (300 - 1000 C) than can be imaged with conventional thermal imaging systems in the 3 - 5 μm range or in visible. Figure 17 shows the comparison of visible and infrared images of the Mount Kilauea Volcano in, Hawaii. The infrared image of the volcano clearly shows a hot lava tube running underground which is not visible to the naked eye.

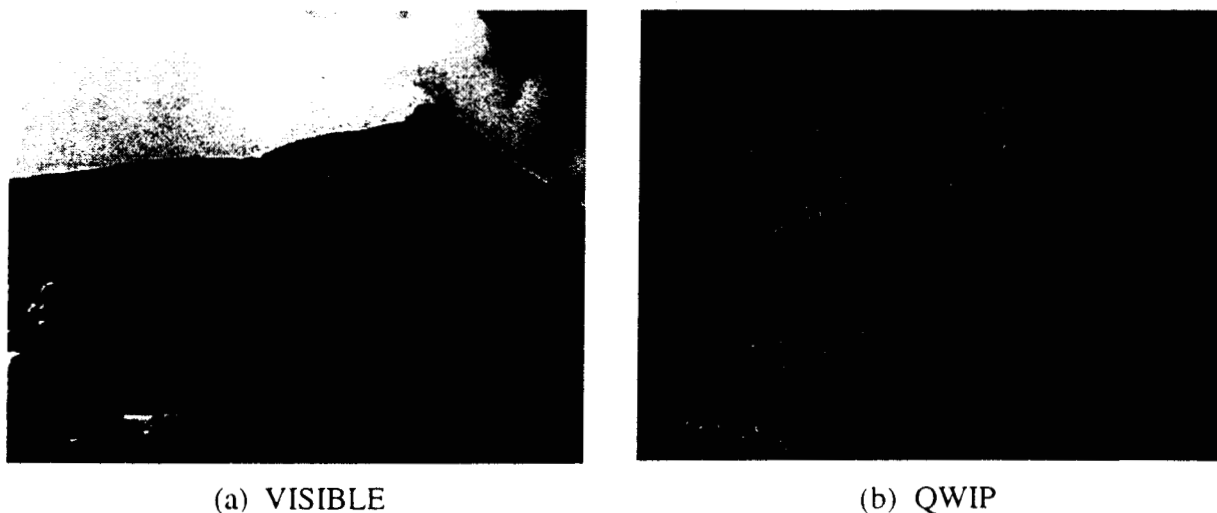


Fig. 17. Comparison of visible and infrared images of the Mount Kilauea Volcano in, Hawaii. (a) Visible image from a highly sensitive CCD camera. (b) Image from the 256x256 portable QWIP camera. The wide dynamic range enabled us to image volcanic features at temperatures much higher (300 - 1000 C) than can be imaged with conventional thermal imaging systems in the 3 - 5 μm range or in visible. The infrared image of the volcano clearly show a hot lava tube running underground which is not visible to the naked eye. This demonstrates the advantages of long wavelength infrared in geothermal mapping.

MEDICINE:

This QWIP RADIANCE camera had limited exposure in the medical community as well. A group of researchers from the State University of New York in Buffalo and Walter Reed Army Institute of Research in Washington DC has used in the Dynamic Area Telethermometry (DAT). DAT has been used to study the physiology and patho-physiology of cutaneous perfusion, which has many clinical applications. DAT involves accumulation of hundreds of consecutive IR images and fast Fourier transform (FFT) analysis of the biomodulation of skin temperature, and of the microhomogeneity of skin temperature (HST, which measures the perfusion of the skin's capillaries). The FFT analysis yields the thermoregulatory frequencies and amplitudes of temperature and HST modulation. To obtain reliable DAT data, one needs an IR camera in the $>8\text{ }\mu\text{m}$ range (to avoid artifacts of reflections of modulated emitters in the environment) a repetition rate of 30 Hz (allowing accumulation of a maximal number of images during the observation period (to maximize the resolution of the FFT), frame to frame instrumental stability (to avoid artifact stemming from instrument modulation) and sensitivity of less than 50 mK. According to these researchers the longer wavelength operation, higher spatial resolution, higher sensitivity and greater stability of the QWIP RADIANCE made it the best choice of all IR cameras.

This camera has also been used by a group of researchers at the Texas Heart Institute in a heart surgery experiment performed on a rabbit heart. This experiment clearly revealed that it is possible to detect arterial plaque built inside a heart by thermography. Figure 18 clearly shows arterial plaque accumulated in a rabbit heart.

DEFENSE:

It is not necessary to explain how real time IR imaging is important in surveillance, reconnaissance and military operations. The QWIP RADIANCE was used by the researchers at the Ballistic Missile Defense Organization's innovative science and technology experimental facility in a unique experiment to

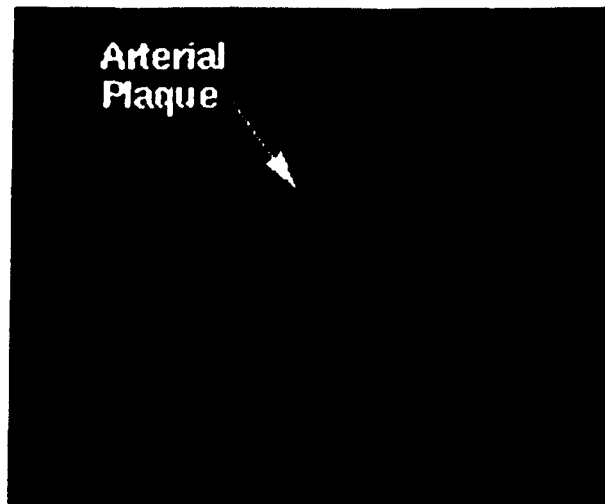


Fig. 18. This image shows arterial plaque deposited in a rabbit heart.

discriminate and clearly identify the cold launch vehicle from its hot plume emanating from rocket engines.

DEFENSE:

It is not necessary to explain how real time IR imaging is important in surveillance, reconnaissance and military operations. The QWIP RADIANCE was used by the researchers at the Ballistic Missile Defense Organization's innovative science and technology experimental facility in a unique experiment to discriminate and clearly identify the cold launch vehicle from its hot plume emanating from rocket engines.

Usually, the temperature of cold launch vehicles is about 250°C, whereas the temperatures of the hot plume emanating from launch vehicle can reach 950°C. According to the Planck's blackbody emission theory, the photon flux ratio of 250°C and 950°C blackbodies at 4 μm is about 25,000, whereas the same photon flux difference at 8.5 μm is about 115 (see Figure 19). Therefore, it is very clear that one must explore longer wavelengths for better cold-body versus hot plume discrimination, because the highest instantaneous dynamic range of IR cameras is usually 12-bits (i.e., 4096) or less. Figure 20 shows a

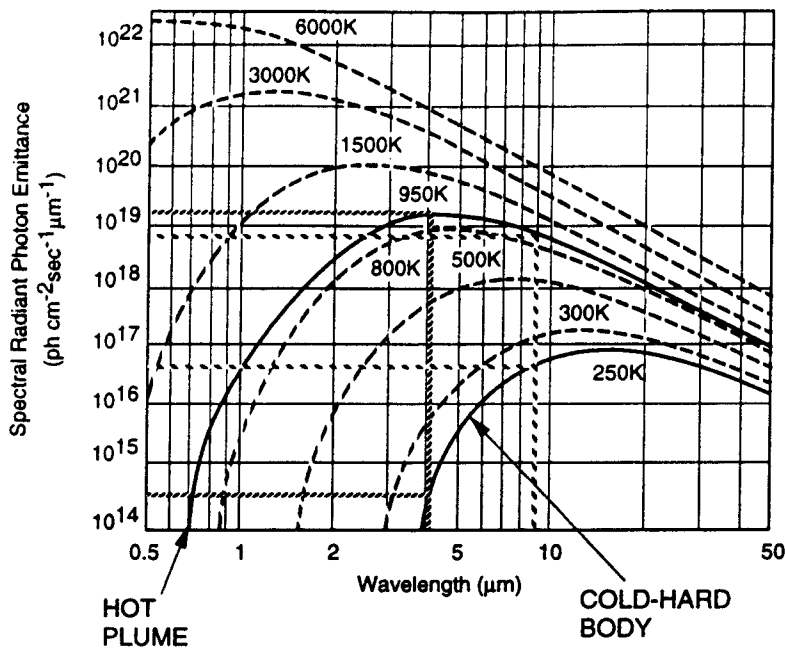


Fig. 19. Blackbody spectral radiant photon emittance at various temperatures.

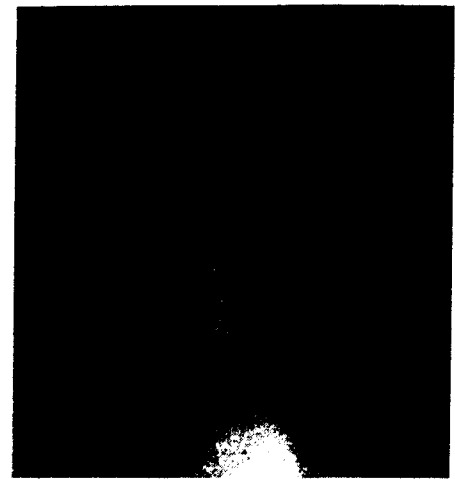


Fig. 20. Image of a Delta-II launch vehicle taken with the long-wavelength QWIP RADIANCE during the launch. This clearly indicates the advantage of long-wavelength QWIP cameras in the discrimination and identification of cold launch vehicles in the presence of hot plume during early stages of launch.

image of Delta-II launch taken with QWIP RADIANCE camera. This clearly indicates the advantage of long-wavelength QWIP cameras in the discrimination and identification of cold launch vehicles in the presence of hot plume during early stages of launch.

ASTRONOMY:

In this section we discuss the first astronomical observations with a QWIP FPA. In order to perform this astronomical observation we have design a QWIP wide-field imaging multi-color prime focus infrared camera (QWICPIC). Observations were conducted at the five meter Hale telescope at Mt. Palomar with QWICPIC based on 8-9 μm 256x256 QWIP FPA operating at $T=35\text{ K}$. The ability of QWIPs to operate under high photon backgrounds without excess noise enables the instrument to observe from the prime focus with a wide $2' \times 2'$ field of view, making this camera unique among the suite of infrared instruments

available for astronomy. The excellent $1/f$ noise performance (see Figure 21) of QWIP FPAs allows QWICPIC to observe in a slow scan strategy often required in infrared observations from space.

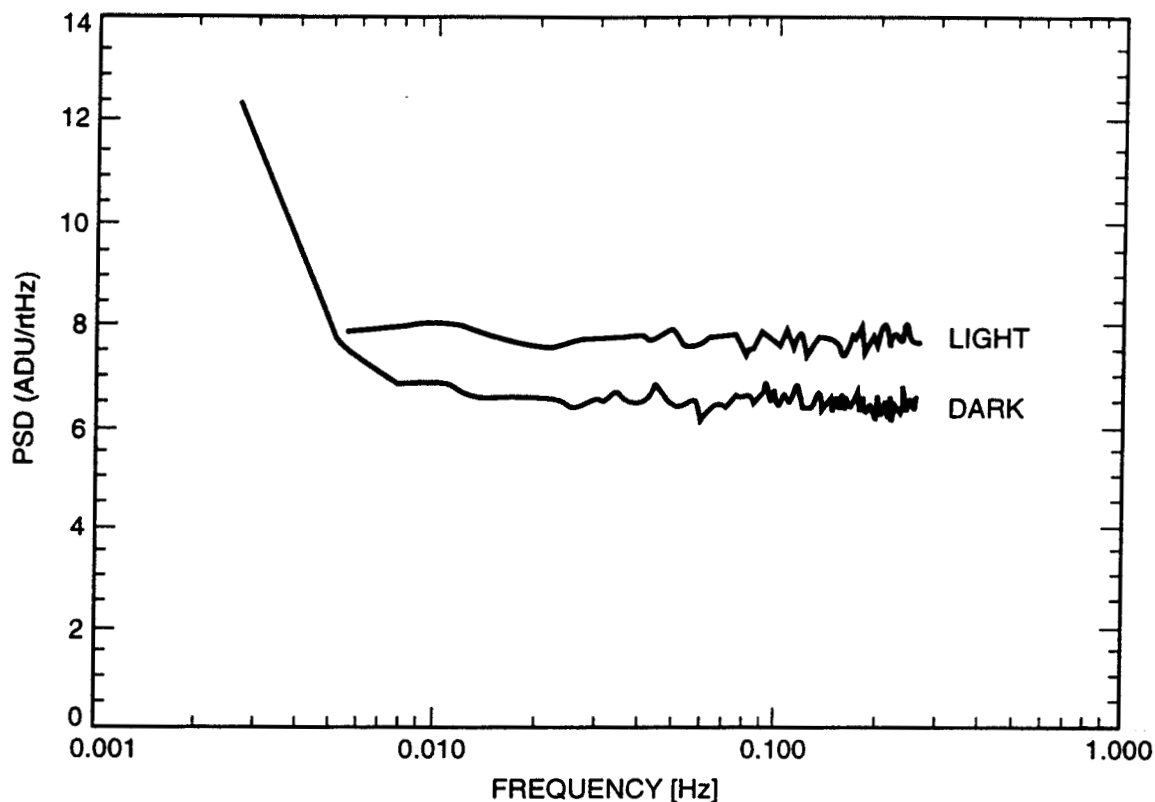


Fig. 21. $1/f$ noise spectrum of 8-9 μm 256x256 QWIP focal plane array. (1 ADU = 430 electrons). This clearly shows that QWIPs have no $1/f$ down to 30 mHz. This allows QWIP based instruments to use longer integration times and frame adding capability.

12. SUMMARY

In summary, we have demonstrated 15 micron cutoff 128x128 QWIP FPA camera, hand-held and palmsize 256x256 long-wavelength QWIP cameras and 648x486 long-wavelength camera, and several applications in science, medicine and defense. In addition, we have demonstrated MWIR:LWIR, LWIR:VWIR dualband QWIP detectors, and long-wavelength ($\lambda_c = 10 \mu\text{m}$) GaAs based QWIPs with detectivities sufficient for low background applications.

13. ACKNOWLEDGMENTS

The research described in this paper was performed by the Center for Space Microelectronics Technology, Jet Propulsion Laboratory, California Institute of Technology, and was jointly sponsored by the JPL Director's Research and Development Fund, the Ballistic Missile Defense Organization / Innovative Science & Technology Office, the National Aeronautics and Space Administration, Office of Space Science, and Air Force Research Laboratory.

14. REFERENCES

- [1] M. T. Chahine, "Sensor requirements for Earth and Planetary Observations," *Proceedings of Innovative Long Wavelength Infrared Detector Workshop*, Pasadena, California, pp. 3-31, April 24-26, 1990.
- [2] D. Duston, "BMDO's IS&T faces new hi-tech priorities", *BMD Monitor*, pp 180-183, May 19, 1995.
- [3] S. D. Gunapala and K. M. S. V. Bandara, *Physics of Thin Films*, Academic Press, **21**, 113 (1995).
- [4] S. D. Gunapala, J. S. Park, G. Sarusi, T. L. Lin, J. K. Liu, P. D. Maker, R. E. Muller, C. A. Shott, T. Hoelter, and B. F. Levine "128 x 128 GaAs/Al_xGa_{1-x}As Quantum Well Infrared Photodetector Focal Plane Array for Imaging at 15 μ m," *IEEE Trans. Electron Devices*, **44**, pp. 45-50, 1997.
- [5] Sarath D. Gunapala, John K. Liu, Jin S. Park, Mani Sundaram, Craig A. Shott, Ted Hoelter, True-Lon Lin, S. T. Massie, Paul D. Maker, Richard E. Muller, and Gabby Sarusi" 9 μ m Cutoff

256x256 GaAs/Al_xGa_{1-x}As Quantum Well Infrared Photodetector Hand-Held Camera", IEEE Trans. Electron Devices, **44**, pp. 51-57, 1997.

- [6] S. V. Bandara, S. D. Gunapala, J. K. Liu, E. M. Luong, J. M. Mumolo, W. Hong, D. K. Sengupta and M. J. McKelvy, "10 - 16 mm broad-band quantum well infrared photodetector", to be published in Appl. Phys. Lett., 1998.
- [7]. Grave, A. Shakouri, N. Kuze, and A. Yariv, "Control of electric field domain formation in multiquantum well structures", Appl. Phys. Lett. **63**, 1101 (1993).
- [8]. Ting Mei, G. Karunasiri, and S. J. Chua, "Two-color infrared detection using intersubband transitions in multiple step quantum wells with superlattice barriers", Appl. Phys. Lett. **71**, 2017 (1997).
- [9] Ph. Bois, E. Costard, J. Y. Duboz, J. Nagle, E. Rosencher and B. Vinter, "Optimized multiquantum well infrared detector", SPIE proceedings 2552, Infrared Technology XXI, pp. 755, 1995.
- [10] M. Z. Tidrow, J. C. Chiang, Sheng S. Li, K. Bacher, "A high strain two-stack two-color quantum well infrared photodetector", Appl. Phys. Lett. **70**, pp. 859, 1997.
- [11] B. F. Levine, C. G. Bethea, G. Hasnain, V. O. Shen, E. Pelve, R. R. Abbott, and S. J. Hsieh, Appl. Phys. Lett., **56**, 851 (1990).
- [12] S. D. Gunapala, T. N. Krabach, S. V. Bandara, J. K. Liu, and M. Sundaram, "Applications of Long-wavelength 256x256 Quantum Well Infrared Photodetector (QWIP) Hand-held Camera", SPIE proceedings 3061, Infrared Technology and Applications XXIII, pp. 292, 1997.